

The UV continua and inferred stellar populations of galaxies at $z \simeq 7 - 9$ revealed by the Hubble Ultra Deep Field 2012 campaign

J.S. Dunlop^{1*}, A.B. Rogers¹, R.J. McLure¹, R.S. Ellis², B.E. Robertson³, A. Koekemoer⁶, P. Dayal¹, E. Curtis-Lake¹, V. Wild^{1,4}, S. Charlot⁵, R.A.A. Bowler¹, M.A. Schenker², M. Ouchi⁷, Y. Ono⁷, M. Cirasuolo^{1,8}, S.R. Furlanetto⁹, D.P. Stark³, T.A. Targett¹, E. Schneider³.

¹ SUPA†, Institute for Astronomy, University of Edinburgh, Royal Observatory, Edinburgh, EH9 3HJ

² Department of Astrophysics, California Institute of Technology, MS 249-17, Pasadena, CA 91125, USA

³ Department of Astronomy and Steward Observatory, University of Arizona, Tucson, AZ 85721, USA

⁴ School of Physics and Astronomy, University of St Andrews, North Haugh, St Andrews, KY16 9SS

⁵ UPMC-CNRS, UMR7095, Institut d'Astrophysique de Paris, F-75014, Paris, France

⁶ Space Telescope Science Institute, Baltimore, MD 21218, USA

⁷ Institute for Cosmic Ray Research, University of Tokyo, Kashiwa City, Chiba 277-8582, Japan

⁸ UK Astronomy Technology Centre, Royal Observatory, Edinburgh, EH9 3HJ

⁹ Department of Physics & Astronomy, University of California, Los Angeles, CA 90095, USA

24 October 2018

ABSTRACT

We use the new ultra-deep, near-infrared imaging of the Hubble Ultra-Deep Field (HUDF) provided by our UDF12 *Hubble Space Telescope* (HST) WFC3/IR campaign to explore the rest-frame ultraviolet (UV) properties of galaxies at redshifts $z > 6.5$. We present the first unbiased measurement of the average UV power-law index, $\langle\beta\rangle$, ($f_\lambda \propto \lambda^\beta$) for faint galaxies at $z \simeq 7$, the first meaningful measurements of $\langle\beta\rangle$ at $z \simeq 8$, and tentative estimates for a new sample of galaxies at $z \simeq 9$. Utilising galaxy selection in the new F140W (J_{140}) imaging to minimize colour bias, and applying both colour and power-law estimators of β , we find $\langle\beta\rangle = -2.1 \pm 0.2$ at $z \simeq 7$ for galaxies with $M_{UV} \simeq -18$. This means that the faintest galaxies uncovered at this epoch have, *on average*, UV colours no more extreme than those displayed by the bluest star-forming galaxies at low redshift. At $z \simeq 8$ we find a similar value, $\langle\beta\rangle = -1.9 \pm 0.3$. At $z \simeq 9$, we find $\langle\beta\rangle = -1.8 \pm 0.6$, essentially unchanged from $z \simeq 6 - 7$ (albeit highly uncertain). Finally, we show that there is as yet no evidence for a significant *intrinsic* scatter in β within our new, robust $z \simeq 7$ galaxy sample. Our results are most easily explained by a population of steadily star-forming galaxies with either \simeq solar metallicity and zero dust, or moderately sub-solar ($\simeq 10 - 20\%$) metallicity with modest dust obscuration ($A_V \simeq 0.1 - 0.2$). This latter interpretation is consistent with the predictions of a state-of-the-art galaxy-formation simulation, which also suggests that a significant population of very-low metallicity, dust-free galaxies with $\beta \simeq -2.5$ may not emerge until $M_{UV} > -16$, a regime likely to remain inaccessible until the *James Webb Space Telescope*.

Key words: galaxies: high-redshift - galaxies: evolution - galaxies: formation - galaxies: stellar populations - cosmology: reionization

1 INTRODUCTION

The revolution in very-deep, near-infrared imaging provided by the 2009 refurbishment of the *Hubble Space Telescope* (HST) with the

Wide Field Camera 3 (WFC3/IR) has enabled the discovery and study of the first substantial samples of galaxies at $z > 6.5$ (see, e.g., Dunlop 2012 for a review). Following the instant success of the initial deep Y_{105} , J_{125} , H_{160} UDF09 imaging (GO 11563; PI: G. Illingworth) of the Hubble Ultra-Deep Field (HUDF; Beckwith et al. 2006) and associated parallel fields (e.g. Oesch et al. 2010; Bouwens et al. 2010a, 2011; McLure et al. 2010, 2011; Finkelstein

* Email: jsd@roe.ac.uk

† Scottish Universities Physics Alliance

et al. 2010; Bunker et al. 2010), WFC3/IR has been used to conduct wider-area surveys for more luminous galaxies at $z = 7 - 8$, both through the CANDELS Treasury programme (Grogin et al. 2011; Koekemoer et al. 2011; Grazian et al. 2012; Oesch et al. 2012), and through parallel imaging programmes such as the BoRG survey (e.g. Bradley et al. 2012). Most recently, attention has been refocussed on pushing to even fainter magnitudes and still higher redshifts, either with the assistance of gravitational lensing (e.g. through the CLASH Treasury Programme; Zheng et al. 2012; Coe et al. 2013), or through our own ultra-deep WFC3/IR imaging in the HUDF (GO 12498; PI: R. Ellis, hereafter UDF12).

Our recently-completed 128-orbit UDF12 observations reach $5-\sigma$ detection limits of $Y_{105} = 30.0$, $J_{125} = 29.5$, $J_{140} = 29.5$, $H_{160} = 29.5$ (after combination with the UDF09 data), and are the deepest near-infrared images ever taken (Ellis et al. 2013). A detailed description of the UDF12 data-set is provided by Koekemoer et al. (2013), and the final reduced images will be available on the team web-page¹.

These new, ultra-deep, multi-band near-infrared images have already yielded the first significant sample of galaxies at $z \simeq 9$, including a possible candidate at $z \simeq 12$ (Ellis et al. 2013). The discovery of galaxies at $z > 8.5$ was a key design goal of this programme, and motivated the first inclusion of deep J_{140} imaging in the HUDF (elsewhere, J_{140} imaging has also played a key role in enabling CLASH to yield convincing galaxy candidates out to $z \simeq 10.7$; Coe et al. 2013). However, the additional deeper H_{160} imaging, and the ultra-deep Y_{105} imaging has also been crucial in enabling the more robust selection of objects at $z \simeq 7$ and $z \simeq 8$ (with improved photometric redshifts; McLure et al. 2013), and a push to still fainter magnitudes. Another key goal of the UDF12 programme was therefore to use the resulting improved samples, coupled with the more accurate 4-band near-infrared photometry, to undertake a new and unbiased study of the rest-frame ultraviolet (UV) spectral energy distributions (SEDs) of faint galaxies at $z > 6.5$.

This paper is thus focussed on revisiting the study of the rest-frame UV SEDs of galaxies, and in particular their UV continuum slopes, β (where $f_\lambda \propto \lambda^\beta$; e.g. Calzetti, Kinney & Storchi-Bergmann 1994; Meurer et al. 1999), armed with the best-available, near-infrared data required for this measurement at $z \simeq 7, 8$ (and, for the first time, at $z \simeq 9$). Because the objects uncovered by HST in the HUDF at these redshifts are too faint for informative near-infrared spectroscopy with current facilities, a broad-band determination of the UV continuum slope β at present offers the only practical way of gaining insight into the rest-frame UV properties of the early populations of galaxies emerging in the young Universe. This (in principle simple, but in practice tricky) measurement is of astrophysical interest for a number of reasons.

First, certainly at more modest redshifts, β has been shown to be a good tracer of dust extinction in galaxies, as it has been demonstrated to be well correlated with excess far-infrared emission from dust (e.g. Meurer et al. 1999; Reddy et al. 2012; Heinis et al. 2013). The reason this works is that (as we again demonstrate later in this paper) an actively star-forming galaxy of \simeq solar metallicity would be expected to display $\beta \simeq -2$ (\equiv zero colour in the AB magnitude system) in the absence of dust, and so any significant deviation to redder values can be viewed as a signature of significant dust extinction (albeit the relation between far-infrared dust-emission and UV-derived dust emission is not expected to be

perfect, given that different regions of the galaxies might be observed in such widely-separated wavelength regimes; e.g. Wilkins et al. 2012; Gonzalez-Perez et al. 2013). These results have been used to interpret the apparent steady progress towards lower average values of $\langle\beta\rangle$ with increasing redshift (from $z \simeq 4$ to $z \simeq 7$) in terms of monotonically-decreasing average dust extinction, with important implications for the inferred cosmological evolution of star-formation activity (e.g. Hathi et al. 2008; Bouwens et al. 2009, 2012; Castellano et al. 2012; Finkelstein et al. 2012).

Second, β is obviously also a function of age (see, for example, Fig. 2 in Rogers, Dunlop & McLure 2013), although (as we explicitly demonstrate later in this paper) the sensitivity is not very strong for young, quasi-continuously star-forming sources, and very blue values of β can certainly only be achieved for very young stellar populations.

Third, β can be used as an indicator of metallicity. In practice of course the impact of metallicity and dust extinction can be degenerate for redder values of β , but blue values significantly lower than $\beta \simeq -2$ are an indicator of a low-metallicity stellar population. For example NGC1703, one of the bluest local star-forming galaxies with $\beta \simeq -2.3$, is generally interpreted as being dust-free, with a significantly sub-solar metallicity (Calzetti et al. 1994), as is the low-mass galaxy BX418 at $z \simeq 2.3$ for which Erb et al. (2010) report $\beta = -2.1$, $E(B - V) \simeq 0.02$, and $Z \simeq 1/6 Z_\odot$.

Fourth, β is influenced by the extent to which the emission from the combined photospheres of the stars in a galaxy is ‘contaminated’ by nebular continuum. Nebular continuum emission is significantly redder than the star-light from a very young, low-metallicity stellar population (e.g. Leitherer & Heckman 1995), and so, given other information (e.g. Stark et al. 2013; Labbé et al. 2013) or assumptions, β can in principle be used to estimate (or correct for) the level of nebular emission in a young galaxy. This in turn can set constraints on the inferred escape-fraction (f_{esc}) of Hydrogen-ionizing photons. It is the rate-density of such photons that requires to be estimated to chart the expected progress of cosmic reionization by young galaxies (e.g. Robertson et al. 2010), but such photons are not directly observable during the epoch of reionization.

Thus, as discussed by many authors, there is a strong motivation for attempting to measure β as accurately as possible, but the interpretation of the results can clearly be problematic given the degeneracies involved. Interestingly, however, the degree of complication in interpretation is result-dependent. In particular, as highlighted by Schaerer (2002) and Bouwens et al. (2010b), the discovery of *extremely* blue values of $\beta \simeq -3$ would offer a fairly clean and powerful result, because such values can only be produced by a stellar population which is simultaneously very young, of extremely low metallicity, dust-free, and also free of significant nebular emission (corresponding to a very high escape fraction for ionizing photons). Since these are exactly the combined properties which might be expected of the first galaxies (which possibly commenced the reionization of the Universe; e.g. Paardekoooper, Khochfar & Dalla Vecchia 2013; Mitra, Ferrara & Choudhury 2013) the measurement of β during the first billion years of cosmic time has been a key focus of several recent studies of galaxies at $z \simeq 7$ (Bouwens et al. 2010b, 2012; Dunlop et al. 2012; Finkelstein et al. 2010, 2012; McLure et al. 2011; Wilkins et al. 2011; Rogers, Dunlop & McLure 2013).

However, as discussed in detail by Dunlop et al. (2012) and Rogers et al. (2013), previous attempts to determine the UV spectral slope at faint magnitudes ($M_{UV} > -19$) have inevitably been afflicted by bias. The interested reader is referred to these papers for

¹ <http://udf12.arizona.edu>

detailed discussions and simulations, but there are three key points to consider, each related to photometric scatter and the resulting impact on derived *average* values ($\langle\beta\rangle$).

First, the selection band can bias the result if source selection is pushed to the $5\text{-}\sigma$ limit, and the primary selection band is then also involved in colour determination. For example, imposition of a J_{125} flux density threshold, as applied by Bouwens et al. (2010b), inevitably leads to a blue-bias in the derived average value of $\langle\beta\rangle$ if β is based on $J_{125} - H_{160}$ colour.

Second, the classification of objects as *robust* high-redshift Lyman-break galaxies can also yield a subtle bias towards bluer values of β . Again this is only really an issue for the derivation of average values from individual measurements with substantial photometric scatter. The point is that, while both colour-colour selection (e.g. Bouwens et al. 2010a, 2011) and photometric redshift selection (e.g. McLure et al. 2010, 2011) are sufficiently inclusive to include virtually all plausible star-forming galaxy SEDs at high redshift, photometric scatter can lead to some genuine high-redshift galaxies being misclassified as being at much lower redshift. Because this only happens when the scatter yields erroneously red colours, the result can be clipping of the red end of the *observed* colour distribution, yielding a blue bias in the derived average $\langle\beta\rangle$. Rogers et al. (2013) show that this bias is, unsurprisingly, essentially identical for colour selection and photometric-redshift selection provided *all* galaxies with a plausible high-redshift photometric solution are retained in the latter approach. If attention is confined to the most robust photometrically-selected high-redshift galaxies, then the bias is unfortunately inevitably more extreme (because a very blue colour longward of the putative Lyman break essentially guarantees a robust high-redshift solution; see Dunlop et al. 2012).

Third, if, as advocated by Finkelstein et al. (2012), β is derived from galaxy spectral energy distribution (SED) models (e.g. Bruzual & Charlot 2003; hereafter BC03), the result can be a red bias in $\langle\beta\rangle$. At first sight, the use of galaxy SEDs seems sensible, but the problem is that model galaxy SEDs never produce β significantly bluer than $\beta \simeq -3$. While there is good reason to believe that real galaxy SEDs can never actually yield β significantly bluer than $\beta \simeq -3$, if one wants to compute a population average from a photometrically-scattered set of objects, it is (as already emphasized) important not to artificially clip one end of the *observed* distribution. In this case the effect of insisting on fitting plausible galaxy SEDs is to clip the blue end of the distribution, because any object which displays, say, $\beta = -5$ will be corrected back to $\beta = -3$ (or whatever the most extreme β contained in the galaxy SED library happens to be). The result is a red bias in the average $\langle\beta\rangle$. Thus, as explicitly demonstrated by Rogers et al. (2013), the most robust way to determine an unbiased value of $\langle\beta\rangle$ is via a pure power-law fit to the appropriate photometry.

The primary aim of this paper is not to revisit these bias issues but, rather, to use the new, deep, multi-band near-infrared photometry provided by the UDF12 WFC3/IR imaging campaign to avoid them, and deliver the first straightforward, unbiased measurement of $\langle\beta\rangle$ for faint galaxies at $z \simeq 7$ (comparable to, but somewhat fainter than the luminosity regime where $\langle\beta\rangle \simeq -3$ was originally claimed by Bouwens et al. 2010b). The UDF12 campaign was, in part, designed with this goal in mind. First, the increase in depth and the addition of an extra passband J_{140} allows significantly more accurate measurements of UV slope down to $M_{UV} \simeq -17$. Second, the introduction of the deep J_{140} imaging allows object selection to be based primarily on a band which has minimal influ-

ence on derived UV slope (whether derived by $J_{125} - H_{160}$ colour, or by power-law fitting through J_{125} , J_{140} , H_{160}).

A second aim of this paper is then to exploit both the new UDF12 photometry, and the new $z \simeq 8$ and $z \simeq 9$ galaxies uncovered by McLure et al. (2013) and Schenker et al. (2013) in our UDF12 programme (Ellis et al. 2013; Koekemoer et al. 2013), to present the first meaningful measurements of $\langle\beta\rangle$ at $z \simeq 8$ and $z \simeq 9$. Inevitably these first results on β at even higher redshift apply to somewhat brighter absolute magnitudes ($M_{UV} \simeq -18$) than the faintest bin explored at $z \simeq 7$, but nevertheless it is of interest to explore the behaviour of β back to within $\simeq 0.5$ Gyr of the big bang. Measurements of β at even earlier epochs will not be possible until the launch of the *James Webb Space Telescope* (JWST) and the advent of ground-based Extremely Large Telescopes (ELTs).

Finally, a third aim of this paper is to attempt to move beyond the determination of $\langle\beta\rangle$ at $z \simeq 7$, and explore whether the improved accuracy of individual measurements of β afforded by the UDF12 data provide any evidence for a significant intrinsic scatter in β at $z \simeq 7$. The impact of UDF12 on the evidence for a colour-magnitude relation, and its potential evolution over a broader redshift range $z \simeq 4$ to $z \simeq 7$ will be considered in a separate paper (Rogers et al., in preparation).

This paper is structured as follows. In Section 2 we briefly summarize the new UDF12+UDF09 dataset, and the way in which our new high-redshift galaxy samples spanning the redshift range $6.5 < z < 12$ have been selected. Then, in Section 3 we present straightforward (but now essentially unbiased) ‘traditional’ colour measurements of β at $z \simeq 7$ (to aid comparison with previous studies) and also for the first time at $z \simeq 8$ and $z \simeq 9$. In Section 4 we then present our ‘best’ measurements of β based on the multi-band power-law fitting as developed and advocated in Rogers et al. (2013). Here we also draw on the results of our simulations to demonstrate the absence of any substantial bias in our measurements, and to correct for any minor residual effects. We consider the astrophysical implications of our results in Section 5, including a comparison with the predictions of the latest hydrodynamical models of galaxy evolution. Finally our conclusions are summarized in Section 6. All magnitudes are quoted in the AB system (Oke 1974) and any cosmological calculations assume $\Omega_M = 0.3$, $\Omega_\Lambda = 0.7$, and $H_0 = 70 \text{ kms}^{-1} \text{ Mpc}^{-1}$.

2 GALAXY SAMPLES

2.1 UDF12 high-redshift galaxy sample selection

New HUDF galaxy samples were selected from the final UDF12+UDF09 dataset as follows. First, SExtractor (Bertin & Arnouts 1996) was used to select any source which yielded a $> 5\text{-}\sigma$ detection in any one of the final single-band WFC3/IR Y_{105} , J_{125} , J_{140} or H_{160} images, or in any contiguous stacked combination of them (i.e. $Y_{105}+J_{125}$, $J_{125}+J_{140}$, $J_{140}+H_{160}$, $Y_{105}+J_{125}+J_{140}$, $J_{125}+J_{140}+H_{160}$, $Y_{105}+J_{125}+J_{140}+H_{160}$). The catalogues from these ten alternative detection runs were next merged to form a parent sample which was then culled by rejecting any source which showed a $> 2\text{-}\sigma$ detection in any of the three shortest-wavelength (B_{435} , V_{606} , i_{775}) deep HST ACS optical images of the HUDF. This process means that the resulting galaxy sample should remain complete beyond $z = 6.4$ (although it will also yield some galaxies in the redshift range $z \simeq 6 - 6.4$; see McLure et al. 2011, 2013).

Multi-band aperture photometry was then performed at the position of each object (as determined from the detection image which

yielded the highest signal:noise ratio detection), using ‘matched’ circular apertures designed to contain 70% of the flux density from a point source. The appropriate aperture diameters as used are 0.5 arcsec at H_{160} , 0.47 arcsec at J_{140} , 0.44 arcsec at J_{125} , 0.40 arcsec at Y_{105} , and 0.3 arcsec for the ACS z_{850} photometry. The WFC3/IR and z_{850} photometry was then all aperture-corrected to 82% of total to correctly match the photometric limits achieved for point sources in the bluer ACS bands within a 0.3-arcsec diameter aperture. In addition, *Spitzer* IRAC photometry at 3.6 and 4.5 μm was included for each source. This was based on a new deconvolution analysis of the deepest available IRAC HUDF imaging (Labbé et al. 2012) using the method described by McLure et al. (2011), and the final UDF12 H_{160} image as the best available template for the galaxies to be fitted to the sky as seen in the highly-confused IRAC imaging. In practice, for all but a few sources, this yielded formal non-detections.

Photometric redshifts (with associated probability distributions) were then derived on the basis of this 10-band photometry, using the method described in McLure et al. (2011). Specifically, a wide range of galaxy SEDs from the BC03 models were utilised, limited only by insisting that galaxy ages were younger than the age of the Universe at each redshift) and dust extinction was allowed to float as high as $A_V = 4$. All flux-density measurements were utilised in this model fitting, even in bands where sources were undetected (including negative flux-density where measured, thus ensuring a consistent derivation of χ^2).

On the basis of the SED fitting, the sample was further refined by retaining only those sources which displayed a statistically-acceptable solution at $z > 6.4$ (i.e. redshift solutions with a formally acceptable value of χ^2 , in practice $\chi^2 < 15$). At this stage all remaining candidates were visually inspected, and rejected from the catalogue if they lay too near the perimeter of the imaging, or too close to bright sources for reliable photometry (a cull that is reflected in the effective survey areas utilised by McLure et al. 2013 in the luminosity function analysis presented therein). A final visual check was also performed to remove any object which yielded a significant detection in a smoothed, stacked $B_{435}+V_{606}+i_{775}$ pseudo broad-band optical ACS image (in order to further minimize the number of low-redshift galaxy contaminants).

Finally, as in Dunlop et al. (2012), all of the ACS+WFC3/IR+IRAC SED fits were inspected, and the sources classified as ROBUST or UNCLEAR depending on whether the secondary, low-redshift solution could be excluded at $>2\text{-}\sigma$ significance, as judged by $\Delta\chi^2 > 4$ between the secondary and primary redshift solution. The final result of this process is a sample of 146 sources, of which 97 are labelled as ROBUST and 49 are UNCLEAR. Absolute rest-frame UV magnitudes at $\lambda_{rest} \simeq 1500 \text{ \AA}$ (M_{1500}) have been calculated for all objects by integrating the spectral energy distribution of the best-fitting evolutionary synthesis model through a synthetic ‘narrow-band’ filter of rest-frame width 100 \AA (see McLure et al. 2011).

2.2 Further sample refinement for β analysis

For the specific purpose of the UV continuum slope analysis presented in this paper, the sample was then split into three redshift bins, yielding 116 galaxies at $z \simeq 7$ ($6.4 < z < 7.5$), 24 galaxies at $z \simeq 8$ ($7.5 < z < 8.5$) and 6 galaxies at $z \simeq 9$ ($8.5 < z < 10$). Finally, to minimize any bias in β introduced at the galaxy-selection stage, we decided to limit the final galaxy catalogues at $z \simeq 7$ and $z \simeq 8$ to those objects which yielded a $>5\text{-}\sigma$ detection in the J_{140} band alone (i.e. $J_{140} < 29.5$ in the 0.47-arcsec diameter aperture).

This reduced the number of galaxies in each sub-sample to 45 at $z \simeq 7$ and 12 at $z \simeq 8$, but still allows us to probe galaxy luminosities down to $M_{UV} \simeq -17$ at $z \simeq 7$. This also means that we are here exploiting the extra depth of the additional UDF12 Y_{105} and H_{160} imaging primarily for the determination of more accurate measurements of β , rather than to push the detection threshold to the absolute limit. This somewhat conservative approach has the beneficial side-effect of reducing the fraction of UNCLEAR galaxies in the final sample to only $\simeq 10\%$, minimizing the need to consider the differences between analyses based on total or ROBUST-only samples.

All derived numbers, plots, and simulations presented hereafter assume the application of this J_{140} threshold at $z \simeq 7$ and $z \simeq 8$. However, at $z \simeq 9$, application of this threshold leaves only 2 objects, and so we do not apply it. In any case, as outlined in Section 3.2, by $z \simeq 9$, J_{140} is the bluest band involved in the β estimation, and so its usefulness as an unbiased band for galaxy selection disappears. For this and other obvious reasons, the results we present on $\langle\beta\rangle$ at $z \simeq 9$ are treated separately, and should be regarded only as tentative/indicative (as compared to the statistically-robust results we now provide at $z \simeq 7$ and $z \simeq 8$).

3 TWO-BAND MEASUREMENT OF UV SLOPES

The standard convention is to characterise the rest-frame UV continuum slope via a power-law index, β , where $f_\lambda \propto \lambda^\beta$. For objects at $z \simeq 7$, the Y_{105} -band photometry could, in principle, be contaminated by Lyman- α emission-line flux, and so it has been common practice to limit the measurement of β at $z > 6.5$ to an estimator based on $J_{125} - H_{160}$ colour (e.g. Bouwens et al. 2010b; Dunlop et al. 2012). Now, with the addition of the new J_{140} imaging from the UDF12 campaign, a three-band (J_{125} , J_{140} , H_{160}) power-law fit can be performed at $z \simeq 7$. As quantified in Rogers et al. (2013), a three-band power-law fit is in fact the optimal way to determine β for galaxies in this redshift regime, and so we apply this method for the first time at these redshifts in Section 4. However, to facilitate comparison with previous work, and to see the direct impact of our deeper photometry and our J_{140} galaxy selection on the results, we first perform the standard $J_{125} - H_{160}$ colour estimation of β on our new UDF12 J_{140} filtered sample. Moreover, at $z \simeq 9$, only J_{140} and H_{160} are capable of sampling the continuum longward of $\lambda_{rest} \simeq 1215 \text{ \AA}$, and so β has to be based upon $J_{140} - H_{160}$ colour, rendering power-law fitting once again essentially redundant.

The effective wavelengths of the filters of interest in this study are $J_{125}:\lambda_{\text{eff}}=12486\text{\AA}$, $J_{140}:\lambda_{\text{eff}}=13923\text{\AA}$, and $H_{160}:\lambda_{\text{eff}}=15369\text{\AA}$. We note that these are the ‘pivot’ wavelengths, incorporating not only the filter transmission profiles, but also the full throughput of WFC3/IR including detector sensitivity as a function of wavelength. There are of course a number of definitions of ‘effective wavelength’ for broad-band filters, but the ‘pivot’ wavelength is the appropriate one for the present study, and in any case agrees with the alternative ‘mean’ (source independent) wavelength of the filter to within better than 1% (see, for example, Tokunaga & Vacca 2005).

Adopting the above effective wavelengths, the appropriate equations for converting from near-infrared colour to β are simply

$$\beta = 4.43(J_{125} - H_{160}) - 2 \quad (1)$$

for measurements at $z \simeq 7 - 8$ based on $J_{125} - H_{160}$ colour, and

$$\beta = 9.32(J_{140} - H_{160}) - 2 \quad (2)$$

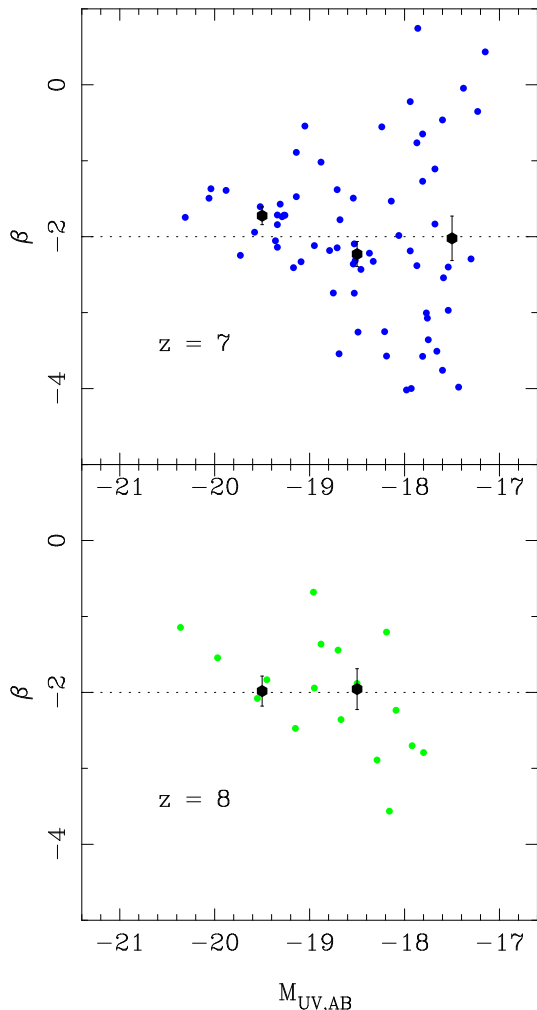


Figure 1. Individual measurements of UV continuum slope, β , at $z \simeq 7$ (upper panel, blue points) and at $z \simeq 8$ (lower panel, green points) for the galaxies in the new UDF12 samples (as detailed in Section 2.2) plotted versus their UV absolute magnitudes ($M_{UV,AB} \equiv M_{1500}$). The values of β shown here are derived from the UDF12 data using $J_{125} - H_{160}$ colours as described in Section 3. The average values, along with standard errors in the mean, are plotted (in black) for each 1-magnitude wide luminosity bin which contains > 5 sources (see also Table 1). The UDF12 galaxy samples used have been confined to those objects which are detected at $> 5\sigma$ in the J_{140} -band, in order to minimize colour bias in the selection process (J_{140} photometry is not used here in the determination of β). To help provide dynamic range, the samples at $M_{UV,AB} < -19$ have been supplemented with $> 8\sigma$ objects from the UDF09P1 and UDF09P2 parallel WFC3/ACS fields. Errors for individual β measurements are not shown, simply because the typical error can be judged directly from the scatter in the plot (which, it transpires, is effectively all due to photometric error; see Section 4.3). The β values for the individual objects are provided in Table A1.

for measurements at $z > 8.5$ which have to be based purely on $J_{140} - H_{160}$.

As already noted by Dunlop et al. (2012), equation (1) differs very slightly from the relation adopted by Bouwens et al. (2010b), which is $\beta = 4.29(J_{125} - H_{160}) - 2$ (presumably due to the adoption of slightly different effective wavelengths). However, the differences in derived values of β are completely insignificant in the current context (e.g. for $J_{125} - H_{160} = -0.2$, the Bouwens et al. relation yields $\beta = -2.86$, while equation (1) yields $\beta = -2.89$).

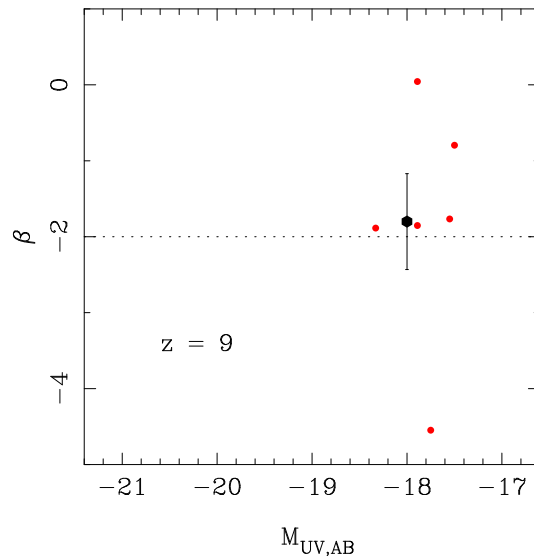


Figure 2. Individual measurements of UV continuum slope, β , (red points) as derived from our UDF12 data using $J_{140} - H_{160}$ colour for the 6 galaxies at $z \simeq 9$ ($8.5 < z < 10$; Ellis et al. 2013), plotted against their UV absolute magnitudes ($M_{UV,AB} \equiv M_{1500}$). The average value, $\langle \beta \rangle$, at $M_{UV} \simeq -18$ is indicated by the black point, with the error-bar corresponding to the standard error in the mean (see Table 1). This is the first attempt at such a measurement at this redshift, and the $J_{140} - H_{160}$ colour does not span a very large wavelength baseline. Moreover, with such a small sample at $z \simeq 9$, the statistical average is clearly not very robust. Nevertheless, the available information suggests that $\langle \beta \rangle$ at $M_{UV,AB} = -18$ at $z \simeq 9$ has not changed dramatically from $z \simeq 7$, and is still consistent with $\beta = -2$.

Finally, we caution that equation (2) must be regarded with some scepticism. First, the relatively short wavelength-baseline provided by $J_{140} - H_{160}$ colour is reflected in the rather large coefficient by which colour (and hence also uncertainties in colour) must be multiplied to yield an estimate of β . Second, whereas J_{125} and H_{160} provide independent samples of a galaxy SED, the J_{140} and H_{160} bands overlap, and hence the resulting measurements are inevitably correlated to some extent. For both these reasons equation (1) should be utilised rather than equation (2) whenever possible. Nevertheless, out of curiosity, in Section 3.2 below we apply equation (2) to the 6 objects in the $8.5 < z < 10$ sample to obtain a first direct observational estimate of $\langle \beta \rangle$ in this previously unexplored redshift regime.

3.1 Robust measurements at $z \simeq 7$ and $z \simeq 8$

In Fig. 1 we show the results of our new $J_{125} - H_{160}$ colour-based determinations of β for the galaxies in the new UDF12 samples at $z \simeq 7$ and $z \simeq 8$, plotted versus their UV absolute magnitudes ($M_{UV,AB} \equiv M_{1500}$). To help provide dynamic range, the samples at $M_{UV,AB} < -19$ have been supplemented with $> 8\sigma$ objects from the UDF09P1 and UDF09P2 parallel WFC3/ACS fields; the individual measurements for all the UDF12, UDF09P1 and UDF09P2 sources utilised in this analysis are given in the Appendix in Table A1.

In this Fig. 1 we also plot the average values, along with standard errors in the mean, for each 1-magnitude wide luminosity bin which contains > 5 sources. These values are tabulated in Table 1. We emphasize that, in order to minimize colour bias in the selection process, the UDF12 galaxy samples used have been confined

Table 1. Derived average UV continuum slopes, $\langle\beta\rangle$, and standard errors as a function of absolute UV magnitude (in bins with $\Delta M_{UV} = 1$ mag) and redshift. The values given in column two are derived from simple two-band colours as described in Section 3, and are only tabulated for luminosity bins that contain > 5 galaxies from the UDF12 and/or UDF09 Parallel Fields (see Figs 1 and 2). The values given in columns three and four are derived using the power-law fitting technique described in Section 4, and have been corrected for small residual biases as evaluated from the results of the end-to-end source injection, retrieval, and measurement simulations detailed in Section 4.1 (see Figs 3 and 4). The galaxy samples analysed at $z \simeq 7$ and $z \simeq 8$ were restricted to objects detected at $> 5\sigma$ in J_{140} to minimize colour-selection bias, as described in Section 2.2. The galaxy sample at $z \simeq 9$ was not restricted in this way (only 2 out of the 6 objects would remain). We also note that, to further minimize bias, both ROBUST and UNCLEAR objects were retained in evaluating these average values of β , but in practice the J_{140} cut ensures that virtually all objects are ROBUST, and rejection of the 5 UNCLEAR objects at $z \simeq 7$, and the sole UNCLEAR object at $z \simeq 8$ does not significantly change these results. We note that the M_{UV} bin centres quoted here refer to magnitudes based on 82% of enclosed flux density for a point source as detailed in Section 2.1, and are thus $\simeq 0.2$ mag fainter than presumed total M_{UV} for unresolved (or marginally-resolved) sources. Finally, we note that the two-colour and power-law β values for the individual objects are provided in Table A1.

M_{UV}	$\langle\beta\rangle$ ($J - H$) Mean	$\langle\beta\rangle$ (Power-law) Mean	$\langle\beta\rangle$ (Power-law) Weighted Mean
$z \simeq 7$			
-19.5	-1.72 ± 0.12	-1.81 ± 0.12	-1.94 ± 0.12
-18.5	-2.23 ± 0.16	-2.08 ± 0.15	-2.08 ± 0.15
-17.5	-2.02 ± 0.29	-2.08 ± 0.26	-2.03 ± 0.26
$z \simeq 8$			
-19.5	-1.98 ± 0.27	-2.03 ± 0.17	-1.93 ± 0.17
-18.5	-1.96 ± 0.27	-1.88 ± 0.25	-1.84 ± 0.25
$z \simeq 9$			
-18	-1.80 ± 0.63		

to those objects which are detected at $> 5\sigma$ in the J_{140} -band as described in Section 2.2. Moreover, to further minimize bias, both ROBUST and UNCLEAR objects were retained in evaluating these average values of β (see Rogers et al. 2013), but in practice the J_{140} cut ensures that virtually all objects are ROBUST, and rejection of the 5 UNCLEAR objects at $z \simeq 7$, and the sole UNCLEAR object at $z \simeq 8$ does not significantly change these results.

Our success in, for the first time, essentially eliminating any significant colour bias from these measurements at $z \simeq 7$ and $z \simeq 8$ is further confirmed below in Section 4, by the power-law β determinations and associated end-to-end data simulations. Our new, robust results at $z \simeq 7$ confirm and extend the main conclusion of Dunlop et al. (2012), that there is, as yet, no evidence for UV continua significantly bluer than $\beta \simeq -2$ in the currently detectable galaxy population at $z \simeq 7$.

The results presented here at $z \simeq 8$ represent the first, meaningful and unbiased measurement of $\langle\beta\rangle$ for a significant sample of galaxies at this even earlier epoch, but we cannot probe to such faint absolute magnitudes as at $z \simeq 7$. Nevertheless, over the available dynamic range $-20 < M_{UV} < 18$ we clearly see no evidence for any significant change from $z \simeq 7$, with the average UV continuum

slope $\langle\beta\rangle$ again consistent with $\beta = -2$ (the $z \simeq 8$ measurement remains more inaccurate simply due to smaller sample size).

3.2 Preliminary measurements at $z \simeq 9$

In Fig. 2 we show the results of our attempt to determine β for the 6 new galaxies we have uncovered in the HUDF at $8.5 < z < 10$, as reported by Ellis et al. (2013). These measurements are necessarily based on $J_{140} - H_{160}$ colour, and the individual values of β thus derived are indicated by the red points in Fig. 2. The scatter is very large, as expected given the photometric errors and the limitations of equation (2) already discussed above. Nevertheless, since all of these objects have absolute UV magnitudes in the range $-18.5 < M_{UV} < -17.5$ we have proceeded to calculate the average $\langle\beta\rangle$ for a single bin centred at $M_{UV} \simeq -18$. This is shown by the black point, which corresponds to $\langle\beta\rangle = -1.80 \pm 0.63$ (where the error is the standard error in the mean).

Such a measurement has not previously been possible at this redshift, and this first effort clearly yields a highly-uncertain result which should not be over-interpreted. Nevertheless, the current data provide no obvious evidence that $\langle\beta\rangle$ at $M_{UV} = -18$ has changed dramatically between $z \simeq 7$ and $z \simeq 9$, with the average value still fully consistent with $\beta = -2$.

4 POWER-LAW MEASUREMENTS AND DATA ANALYSIS SIMULATIONS

We now proceed to determine β using the power-law fitting method as explored and optimized in Rogers et al. (2013). We have also performed a set of end-to-end data-analysis simulations, starting with the injection of sources into the real UDF12 images, in order to quantify any remaining residual bias in our derived average values of $\langle\beta\rangle$. We first describe these simulations, before proceeding to summarize the results.

4.1 Source injection, retrieval and measurement simulations

Our simulations begin by defining a distribution of UV slopes. For the present study we adopt a delta function at $\beta = -2$ as our reference model, but also consider ‘top hat’ distributions of various widths, as discussed below in Section 4.3.

Next, we create an input catalogue of galaxies with β values drawn from the defined distribution, redshifts in the range $6 < z < 9$, and absolute magnitudes spanning $-22 < M_{UV} < -16$ (with the relative number density of objects at different magnitudes governed by the latest $z = 7$ luminosity function of McLure et al. 2013). A model SED is then created for each galaxy, incorporating the intrinsic colour, the IGM attenuation of flux blueward of the Lyman break, the redshifting of the spectrum into the observed frame, and then cosmological dimming. Empirical PSFs are then created with broad-band flux-densities based on the model SEDs (in practice, the PSFs are set to zero in the $B_{435}, V_{606}, i_{775}$ bands where the flux is entirely attenuated). The PSFs are then inserted into the real multi-wavelength UDF12 images, avoiding existing bright sources and regions of high rms noise where real candidates would be discarded.

Objects are then reclaimed using SExtractor; we accept only objects lying within 2-pixels of an input PSF centre, and then perform aperture photometry on these objects in exactly the same way as for the real galaxies. Photometric redshifts are then obtained using Le Phare (Arnouts et al. 1999; Ilbert et al. 2006) with the same

BC03 models used in the real data analysis. We adopt an identical selection function to that used for the real data, and measure absolute magnitudes with the same synthetic filter on the best-fitting BC03 model. Following Rogers et al. (2013), UV continuum slopes are obtained by performing a power-law fit to the $J_{125}, J_{140}, H_{160}$ flux densities ($Y_{105}, J_{125}, H_{160}$ in the parallel fields, accounting for partial attenuation of the Y -band by the Lyman break where appropriate).

4.2 Results at $z \simeq 7$

In Fig. 3 we show the results of our power-law analysis for the galaxies at $z \simeq 7$, split into the same three luminosity bins as in Fig. 1, and this time, for completeness, showing results for both the FULL (upper row) and ROBUST-source only (lower row) samples. The grid of power-law models fitted to the WFC3/IR photometry extends over a deliberately very large range, $-8 < \beta < 5$, to ensure that the *observed* β distribution is not artificially truncated. However, in practice (primarily due to the J_{140} significance cut) the sample studied here has photometry of sufficient quality that no object yields a measured $\beta < -4$.

The grey histograms in Fig. 3 show the distribution of the power-law derived β values in each bin, and the small squares with error bars indicate the average $\langle \beta \rangle$ values (and associated standard errors). The results derived from the real data are compared here with the results from our reference simulation in which every fake galaxy is assigned $\beta = -2$ before being inserted into the UDF12 imaging; the red histograms indicate the distribution of power-law β values retrieved from the simulations, with the red points indicating the corresponding average and standard error in each luminosity bin. The red points thus offer a measure of the bias in our measurements of average $\langle \beta \rangle$ which can be seen to be negligible for both the FULL and ROBUST samples. As expected, it can be seen that confining the sample to ROBUST sources results in the removal of a few of the redder galaxies in the faintest magnitude bin, but because the number of UNCLEAR sources is so small, the results are essentially unchanged (especially when measured relative to simulation expectation, which also moves slightly blueward in the ROBUST-source simulations).

The final values given for the power-law determination of $\langle \beta \rangle$ at $z \simeq 7$ in Table 1 are taken from the FULL-sample analysis shown in the upper row of Fig. 3, and are calculated relative to the simulated values (to correct for any small residual bias). As long as the appropriate correction is applied, the results are essentially identical if they are derived from the ROBUST-source only analysis presented in the lower row. Within the errors, all three luminosity bins at $z \simeq 7$ are clearly consistent with $\beta = -2$, with a best-estimate of $\langle \beta \rangle = -2.1$ in the fainter two bins. Reassuringly, the power-law estimates are fully consistent with the $J_{125} - H_{160}$ colour-based measurements presented in Section 3 (see Table 1 for details and errors, and Table A1 for individual object measurements).

4.3 Results at $z \simeq 8$

In Fig. 4 we show our power-law β determinations at $z \simeq 8$. The values derived from the real data are again shown by the grey histograms, with the average and standard error indicated by the black squares with error bars. Similarly, the corresponding results for the $\beta = -2$ simulation are indicated in red. At $z \simeq 8$ the J_{140} significance threshold leaves only two galaxies fainter than $M_{UV} = -18$

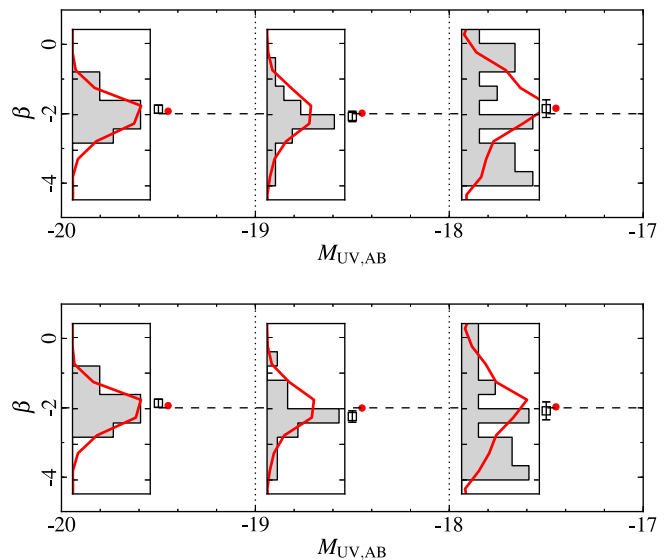


Figure 3. The distribution of individual power-law β measurements at $z \simeq 7$, along with average values, $\langle \beta \rangle$ (and standard errors), plotted against UV absolute magnitude. Results are shown for all sources (upper row), and for ROBUST sources only (lower row). Simulations shown in red are based on 2000 galaxies inserted with $\beta = -2$. The data from UDF12 are shown in grey/black. The data in the brightest two bins have been supplemented with a few sources from the two UDF09 parallel fields as discussed in the text and in the caption to Fig. 1.

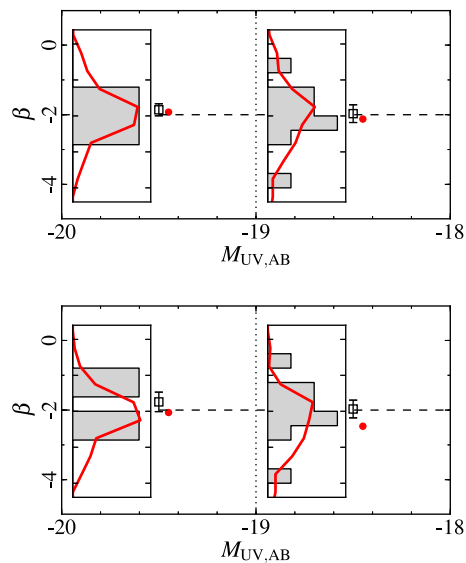


Figure 4. The distribution of individual power-law β measurements at $z \simeq 8$, along with average values, $\langle \beta \rangle$ (and standard errors) plotted against UV absolute magnitude. Results are shown for all sources (upper row), and for ROBUST sources only (lower row). Simulations shown in red are based on 2000 galaxies inserted with $\beta = -2$. The data from UDF12 are shown in grey/black. The faintest bin shown for the $z \simeq 7$ sources in Fig. 3 only contains two sources in our J_{140} -thresholded $z \simeq 8$ sample, and so we do not attempt to show results at $M_{UV} \simeq -17.5$ here. The data in the brighter bin have been supplemented with a few sources from the two UDF09 parallel fields, as discussed in the text and in the caption to Fig. 1.

so, as in Fig. 1, we limit our analysis to the two brighter bins. The samples are smaller, and so the corresponding random errors are larger, but again it can be seen that the values of $\langle\beta\rangle$ derived from the data are consistent with $\beta = -2$ in both luminosity bins, and the blue bias implied from the simulations is relatively modest (although it is slightly larger if only ROBUST objects are retained, as expected).

As at $z \simeq 7$, the final results for the power-law determination of $\langle\beta\rangle$ at $z \simeq 8$ given in Table 1 are derived from the FULL-sample analysis shown in the upper row of Fig. 4, calculated relative to the simulated values. Again, within the errors, both luminosity bins at $z \simeq 8$ are clearly consistent with $\beta = -2$, and the power-law estimates are fully consistent with the $J_{125} - H_{160}$ colour-based measurements presented in Section 3 (see Table 1, and Table A1 for individual object measurements).

4.4 Trends with z , M_{UV} , and evidence for scatter

Our derived average values of $\langle\beta\rangle$ reveal no evidence for a significant trend with redshift over the limited redshift range explored here, $7 < z < 9$. However, it must be remembered that we are currently unable to explore the faintest absolute magnitude bin studied at $z \simeq 7$ at higher redshift.

Our results also do not yield any significant evidence for a relation between $\langle\beta\rangle$ and M_{UV} at a given redshift, although again the available dynamic range is limited, and a full exploration of this issue is deferred to a future paper including results from brighter larger-area surveys.

The one suggestive result that does merit additional scrutiny here is the apparent excess scatter seen in β at the faintest absolute magnitudes probed at $z \simeq 7$. Specifically, in the lowest-luminosity bin plotted in Fig. 3 ($z \simeq 7$, $M_{UV} > -18$) it appears that our simulation (red line in the histogram) does not replicate the observed scatter in β (grey region) as successfully as at brighter magnitudes. It is of interest to attempt to quantify the statistical significance of this effect, as a growth in the intrinsic scatter in β with decreasing luminosity might be expected if, for example, the faintest galaxy samples begin to include a significant number of very young, metal-poor objects.

To do this we have expanded our simulations (beyond a single value of $\beta = -2$) to explore a variety of intrinsic β distributions. In particular, we considered alternative top-hat distributions for the input values of β in order to assess whether a wider intrinsic distribution can provide a significantly improved fit to the data in this faintest bin. To determine the statistical significance of our results, we used a K-S test, as illustrated in the comparison of the simulated and observed cumulative β distributions presented in Fig. 5. For clarity we restrict Fig. 5 to only 3 alternative input models, although for consistency we again show results for the full sample, and for ROBUST sources only. From the K-S test significance values given in Fig. 5 it can be seen that the $\beta = -2$ simulation in fact continues to provide a perfectly acceptable description of the data. Unsurprisingly, a wider intrinsic distribution can provide an improved fit, although the highest significance values are achieved if this distribution remains centred on a value close to $\beta = -2$ (consistent with our results for $\langle\beta\rangle$). Thus, while it is clear that we cannot rule out the possibility that our galaxy sample contains some objects with UV slopes as blue as $\beta \simeq 3$ (see Table A1), the current data certainly do not require any significant intrinsic scatter (even in this well-populated luminosity bin). For now, therefore, reliable conclusions can only be drawn on the basis of population-averaged values, $\langle\beta\rangle$.

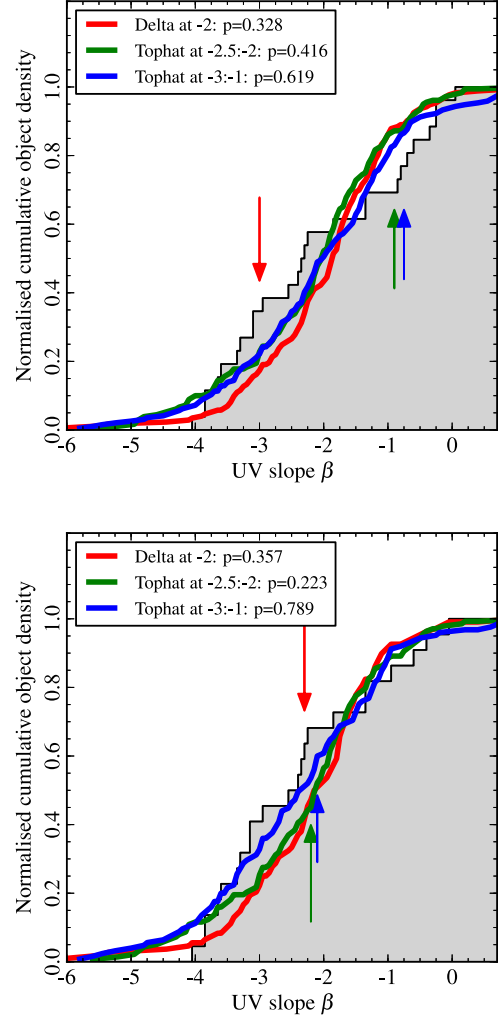


Figure 5. A comparison of the distribution of β values derived for the real galaxies in the faintest luminosity bin probed here at $z \simeq 7$ ($-18 < M_{UV} < -17$), with those predicted by alternative models based on different assumed intrinsic distributions of β . The upper panel shows all sources, while the lower panel contains ROBUST sources only. The grey regions show the cumulative distributions of β as derived from the data, while the coloured lines show the mock cumulative distributions as produced by the output from each alternative simulation. The significance (p) values for each model (under the null hypothesis that the real and simulated distributions are drawn from the same underlying distribution), are given in the top-left corner of each panel. Arrows show where the maximum deviation between the data and each simulation occurs, with the length of the arrow equal to the deviation.

5 DISCUSSION

5.1 Comparison with previous results

At $z \simeq 7$ our results can be compared with the recent work of Bouwens et al. (2012) and Finkelstein et al. (2012), and with our own previous study in Dunlop et al. (2012) which (as with the investigations by Bouwens et al. 2010b, Finkelstein et al. 2010, and Wilkins et al. 2011) was based purely on the portion of UDF09 WFC3/IR imaging obtained prior to the end of 2009.

Based on the complete UDF09 dataset, at $z \simeq 7$, Bouwens et al. (2012) reported a measurement for $\langle\beta\rangle$ at $M_{UV} \simeq -18.25$ of

$\langle\beta\rangle = -2.68 \pm 0.19 \pm 0.28$, with the first error representing the random error, and the second the estimated systematic uncertainty (albeit presumably, in practice, not symmetric). This measurement is larger (redder) than the original Bouwens et al. (2010b) measurement of -3.0 ± 0.2 in the same luminosity bin, with the change being due to the availability of the final UDF09 dataset, improved assessment of bias, and (possibly) the removal of the J_{125} flux-density threshold in the galaxy-selection process (see Rogers et al. 2013). Clearly, however, the Bouwens et al. (2012) result still remains bluer than that reported here at comparable absolute magnitudes, albeit the two can be reconciled within the errors (especially if the estimated systematic error is applied to the red, moving $\langle\beta\rangle$ to $\simeq -2.40$). However, the Bouwens et al. (2012) results could easily still be biased blue in the faintest bin, as they did not have the advantage of the deeper photometry from UDF12 exploited here, nor could the J_{140} significance threshold be applied to assist in the selection of unbiased, secure sub-samples of galaxies. Circumstantial evidence that the faintest measurement of $\langle\beta\rangle$ of Bouwens et al. (2012) remains biased to the blue is offered by the fact that the $\langle\beta\rangle$ value for their next brightest bin is much redder, at $\langle\beta\rangle = -2.15 \pm 0.12 \pm 0.28$, in excellent agreement with our own results at comparable magnitudes.

Finkelstein et al. (2012) have also reported a move to redder values of $\langle\beta\rangle$ for the faintest galaxies at $z \simeq 7$ as found in the final UDF09 dataset compared to the original measurements made by Finkelstein et al. (2010). Specifically, Finkelstein et al. (2010) reported $\langle\beta\rangle = -3.07 \pm 0.51$, while Finkelstein et al. (2012) reported a median value of $\langle\beta\rangle = -2.68^{+0.39}_{-0.24}$ which becomes $\simeq -2.45$ after bias correction. Given the errors, clearly this result, while still somewhat bluer, can be reconciled with our own, now more accurate measurements.

In Dunlop et al. (2012) we aimed to highlight the dangers of the potential for blue bias in the early measurements of $\langle\beta\rangle$ made in the immediate aftermath of the first discovery of faint $z \simeq 7$ galaxies with WFC3/IR. We utilised only the first epoch of the UDF09 dataset, and confined our attention to $> 8\text{-}\sigma$ sources, and therefore did not report a robust result for absolute magnitudes as faint as $M_{UV} \simeq -18.5$ at $z \simeq 7$. We did, however, report $\langle\beta\rangle = -2.12 \pm 0.13$ at $M_{UV} \simeq -19.5$ for $z \simeq 7$ galaxies (in good agreement with the results from Bouwens et al. and Finkelstein et al. discussed above), and found $\langle\beta\rangle = -2.14 \pm 0.16$ at $M_{UV} \simeq -18.5$ for $z \simeq 5 - 6$. Clearly these results are consistent with the values in the corresponding luminosity bins presented here at $z \simeq 7$, confirming the apparent stability of $\langle\beta\rangle$ for the UV-selected population in this high-redshift regime (including the lack of any obvious redshift or luminosity dependence).

Finally, we note that Finkelstein et al. (2012) did attempt a measurement of $\langle\beta\rangle$ at $z \simeq 8$, and found -2.00 ± 0.32 , although this preliminary measurement was not deemed trustworthy enough for inclusion in the abstract (in part because it was substantially redder than at $z \simeq 7$). This result is in fact in very good agreement with the new, more robust determination at $z \simeq 8$ presented here, and indeed seems less surprising given our final results at $z \simeq 7$.

5.2 Physical interpretation

Although we cannot exclude some intrinsic scatter in β , the analysis presented in Section 4.4 shows that we have, as yet, no evidence for it. What is clear is that our derived values of average $\langle\beta\rangle \simeq -2.1 \pm 0.2$ at $z \simeq 7$ clearly exclude the possibility that a large subset of galaxies in our sample have extreme val-

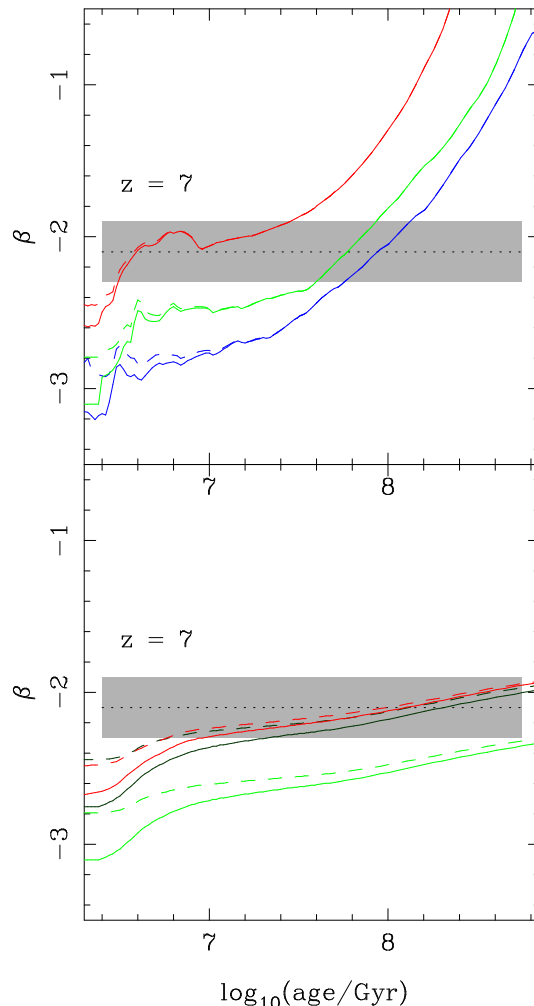


Figure 6. A comparison of our observed average value of $\langle\beta\rangle$ for galaxies with $M_{UV} \simeq -18$ at $z \simeq 7$ with the predicted age-dependence of β from alternative stellar population models with and without nebular emission (with age only plotted up to the age of the Universe at $z \simeq 7$). In both panels our most robust data point is indicated by the horizontal dotted line, with the $1\text{-}\sigma$ uncertainty (standard error) shown by the surrounding grey shaded band. In the *upper panel* the solid lines are derived from instantaneous starburst models, with metallicities of Z_{\odot} (red), $0.2Z_{\odot}$ (green), and $0.02Z_{\odot}$ (blue), assuming zero nebular emission (i.e. $f_{esc} = 1$). The dashed lines are produced by adding nebular continuum emission self-consistently (Robertson et al. 2010), assuming the extreme case $f_{esc} = 0$ (see text for details). In the lower panel we show constant star-formation models, again with and without nebular emission, but this time only for Z_{\odot} (red) and $0.2Z_{\odot}$ (green) models. The dark-green curves show the effect of adding modest dust obscuration/reddening to the $0.2Z_{\odot}$ (brighter green) model, ($\equiv A_V \simeq 0.1$ for SNI dust extinction, or $\equiv A_V \simeq 0.2$ for the extinction law of Calzetti et al. 2000)

ues $\beta \simeq -3$, as anticipated from very young, very low-metallicity, dust-free stellar populations.

To illustrate this, and further explore the consequences of our measurements for the inferred physical properties of the currently-detectable galaxies, we show in Fig. 6 how our results compare with the values expected from stellar populations of different metallicity, nebular emission (related to ionizing escape fraction), dust reddening, and age (up to the age of the Universe at $z \simeq 7$). In this figure our basic, most secure result at $z \simeq 7$ and $M_{UV} \simeq -18$ (which is also consistent with our results at $z \simeq 8$ and $z \simeq 9$) is indicated by

the horizontal dotted line, while the $1\text{-}\sigma$ uncertainty (standard error) is shown by the surrounding grey shaded band (which acceptable models should therefore intercept at plausible ages).

The predictions of β as a function of age shown in Fig. 6 have been produced using the BC03 evolutionary models. Nebular continuum emission has been added to the stellar-population templates self-consistently, based on the flux of Hydrogen-ionising photons predicted from each BC03 model (using the code developed by Robertson et al. 2010). The nebular continuum includes the emission of free-free and free-bound emission by H, neutral He and singly-ionised He, as well as the two-photon continuum of H (see the prescription given in Schaerer 2002).

In the upper panel of Fig. 6 we plot three alternative instantaneous starburst models, with metallicities equal to the solar value Z_{\odot} (red), $0.2Z_{\odot}$ (green), and $0.02Z_{\odot}$ (blue). For each model we show the pure stellar prediction (i.e. zero nebular emission \equiv an ionizing photon escape fraction of unity, $f_{esc} = 1$) as a solid line, and the extreme alternative of maximum nebular contribution (\equiv zero ionizing photon escape fraction, $f_{esc} = 0$) by the dashed line of the same colour. Not surprisingly for these burst models, the impact of the nebular continuum becomes negligible after $\simeq 10$ Myr. During the time period when it is significant, its impact is more pronounced the lower the adopted metallicity (see also figure 4 in Bouwens et al. 2010b).

From Fig. 6 we infer that our results are inconsistent with very young *and* very low metallicity models. Moreover, while $\beta \simeq -2.1$ can be produced by essentially any metallicity at a carefully-selected age, the speed with which the UV continuum reddens with age, coupled with the homogeneity of our results, argues strongly that the burst models illustrated in the upper panel (and in Bouwens et al. 2010b) are inappropriate, and in any case physically unrealistic.

A more natural assumption is that the galaxies selected by our rest-frame UV-selection technique are forming stars quasi-continuously (at least on average, especially at these early times). Therefore, in the lower panel of Fig. 6 we show predictions for constant star-formation models. Again we show the Z_{\odot} (red) and $0.2Z_{\odot}$ (green) models, but this time (for clarity) omit the $0.02Z_{\odot}$ model because, without dust-reddening, the $0.2Z_{\odot}$ model is already too blue until an age of $\simeq 1$ Gyr (and the inferred trend with further reduction in metallicity is clear). Instead, we add a second version of the $0.2Z_{\odot}$ model with modest dust obscuration/reddening ($\equiv A_V \simeq 0.1$ for dust produced by Type-II supernovae (SNII), or $\equiv A_V \simeq 0.2$ for the extinction law of Calzetti et al. 2000). This last curve (in dark green) illustrates the degeneracy between dust extinction and the assumed metallicity of the stellar population.

Clearly, these continuously star-forming models provide a much more plausible explanation of our results, and are capable of delivering the observed homogeneous value of β without any requirement for fine tuning in age (i.e. β is little changed over the relevant timescale, $\simeq 10$ Myr to $\simeq 100$ Myr). One is then left to choose between solar metallicity with very little room for any additional dust reddening, or moderately sub-solar metallicity stellar populations coupled with modest dust reddening. The degeneracies are clear, but the latter scenario is arguably more plausible, and in fact happens to correspond well with the physical properties predicted for the currently observable galaxies (i.e. $M_{UV} < -17$) from the cosmological galaxy-formation simulation discussed below. Finally, we note that while, as expected, the contribution from nebular emission persists to much longer times in these continuously star-forming models, even the extremes adopted here of $f_{esc} = 1$

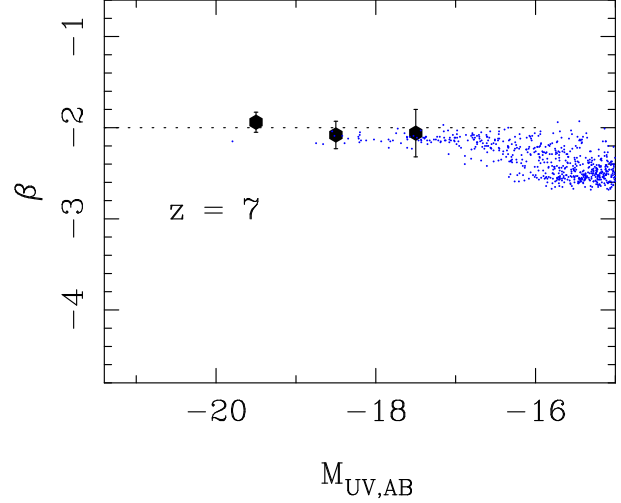


Figure 7. Comparison of our most accurate (bias-corrected power-law) measurements of average $\langle\beta\rangle$ as a function of M_{UV} at $z \simeq 7$ with the predicted β values for individual galaxies as derived from the 10 Mpc cosmological galaxy-formation simulation described in Section 5.3 (see also Dayal et al. 2013). The data plotted here are given in column 4 of Table 1. The model predictions include the effects of dust, and therefore correspond to the predicted *observed* values of β .

and $f_{esc} = 0$ yield unobservably small differences in observed β . Thus, if quasi-continuous star-forming galaxies of modestly sub-solar metallicity are the correct interpretation of our results, there is currently no realistic prospect of estimating f_{esc} from measurements of the UV continuum slope at $z \simeq 7$.

5.3 Comparison with galaxy-formation model predictions

It is instructive to compare our findings with the predictions of a state-of-the-art cosmological galaxy-formation simulation. The simulation used here has been recently described, and its basic observational predictions (e.g. luminosity function, mass function) verified by Dayal et al. (2013). Interested readers are referred to Maio et al. (2007, 2009, 2010) and Campisi et al. (2011) for complete details of the simulation, but the key details can be summarized as follows.

The simulation has been carried out using the TreePM-SPH code GADGET-2 (Springel 2005), within the Λ CDM cosmology given in Section 1, and assuming a baryon density parameter $\Omega_b = 0.04$, a primordial spectral index $n_s = 1$ and a spectral normalisation $\sigma_8 = 0.9$. The periodic simulation box has a comoving size of $10h^{-1}$ Mpc and contains 320^3 DM particles and, initially, an equal number of gas particles. The masses of the gas and DM particles are $3 \times 10^5 h^{-1} M_{\odot}$ and $2 \times 10^6 h^{-1} M_{\odot}$, respectively.

The code includes the molecular chemistry of 13 primordial species: e^- , H, H^- , He, He^+ , He^{++} , H_2 , H_2^+ , D, D^+ , HD, HeH^+ (Yoshida et al. 2003; Maio et al. 2007, 2009), PopIII and PopII/I star formation according to the corresponding initial mass function (IMF; Tornatore, Ferrara & Schneider 2007), gas cooling from resonant and fine-structure lines (Maio et al. 2007) and feedback effects (Springel & Hernquist 2003). The runs track individual heavy elements (e.g. C, O, Si, Fe, Mg, S), and the transition from the metal-free PopIII to the metal-enriched PopII/I regime is determined by the underlying metallicity of the medium, Z , compared with the critical value of $Z_{crit} = 10^{-4} Z_{\odot}$ (see Bromm & Loeb 2003). If $Z < Z_{crit}$, a Salpeter IMF is used, with a mass range

100 – 500 M_{\odot} ; otherwise, a standard Salpeter IMF is used in the mass range 0.1 – 100 M_{\odot} , and a SNII IMF is used for 8 – 40 M_{\odot} (Bromm et al. 2009; Maio et al. 2011).

The chemical model follows the detailed stellar evolution of each SPH particle. At every timestep, the abundances of different species are consistently derived using the lifetime function (Padovani & Matteucci 1993) and metallicity-dependant stellar yields. The yields from SNII, AGB stars, SNIa and pair instability supernovae have been taken from Woosley & Weaver (1995), van den Hoek & Groenewegen (1997), Thielemann et al. (2003) and Heger & Woosley (2002) respectively. Metal mixing is mimicked by smoothing metallicities over the SPH kernel and pollution is driven by wind feedback, which causes metal spreading over \sim kpc scales at each epoch (Maio et al. 2011).

Galaxies are recognized as gravitationally-bound groups of at least 32 total (DM+gas+star) particles by running a friends-of-friends (FOF) algorithm, with a comoving linking-length of 0.2 in units of the mean particle separation. Substructures are identified by using the SubFind algorithm (Springel, Yoshida & White 2001; Dolag et al. 2009) which discriminates between bound and non-bound particles. Of the galaxies identified in the simulation, we only use those that contain at least 10 star particles (at least 145 total particles) in our calculations at $z \simeq 7$. For each such well-resolved galaxy, we obtain the properties of all its star particles, including the redshift of, and mass/metallicity at formation.

Finally, the SED of each galaxy in the simulation snapshot at $z \simeq 7$ is calculated by assuming each star particle forms in a burst and then evolves passively. If, when a star particle forms, the metallicity of its parent gas particle is less than $Z_{crit} = 10^{-4} Z_{\odot}$, we use the PopIII SED (Schaerer 2002); if a star particle forms out of a metal-enriched gas particle ($Z > Z_{crit}$), the SED is computed via the population synthesis code STARBURST99 (Leitherer et al. 1999), using its mass, stellar metallicity, and age. The composite spectrum for each galaxy is then calculated by summing the SEDs of all its star particles, and the intrinsic continuum luminosity, L_c^{int} , is calculated at $\lambda_{rest} = 1500 \text{ \AA}$. We also self-consistently compute the dust mass and attenuation for each galaxy in the simulation box assuming type II SN (SNII) to be the main dust producers (Maiolino et al. 2006; Stratta et al. 2007). The dust mass is converted into an optical depth to UV photons assuming the dust is made of carbonaceous grains spatially distributed as the gas (see Dayal et al. 2010 and Dayal & Ferrera 2012 for complete details of this calculation). The predicted observed UV luminosity is then $L_c^{obs} = L_c^{int} \times f_c$, where f_c is the fraction of continuum photons that escape unattenuated by dust. The intrinsic value of β (β_{int}) is calculated by fitting a power-law through the intrinsic SED of each galaxy over $\lambda_{rest} = 1500 - 3000 \text{ \AA}$ with predicted ‘observed’ β values derived by repeating the power-law fitting after taking into account the dust enrichment and applying the SN extinction curve (Bianchi & Schneider 2007).

In Fig. 7 we show the final predicted ‘observed’ individual values of β for galaxies in this simulation at $z \simeq 7$, plotted against absolute UV magnitude, and compared against our best measurement of the actual (weighted) mean $\langle \beta \rangle$ values at $z \simeq 7$, as given in column 4 of Table 1. Clearly the predictions of this simulation are in good agreement with our new results in a number of ways. First, within the magnitude range probed by our data, the average value of β is basically exactly as predicted. The predicted intrinsic scatter in β at these ‘brighter’ magnitudes is also rather small, perfectly consistent with the analysis presented in Section 4.3. Moreover, the galaxies at $M_{UV} < -17$ in the simulation have moderately sub-solar metallicities (and hence intrinsically blue β values), but their

chemical enrichment history is associated with enough dust to redden the observable values to β values entirely consistent with our average results. Interestingly, this is essentially the same as one of the scenarios we already considered in Section 5.3 as a possible explanation of our observed β values. Finally, the simulation does not yield a significant $\beta - M_{UV}$ relation over the magnitude range probed in the current study, but does reinforce the expectation that the distribution should broaden towards substantially bluer values of β at very faint magnitudes (as a significant population of low-metallicity, dust-free objects finally emerges).

The agreement shown in Fig. 7 may be fortuitous, and a full comparison with alternative galaxy-formation model predictions is beyond the scope of this paper. Nevertheless, Fig. 7 (and the associated physical properties of the simulated galaxies) does provide an interesting perspective on our findings. In particular, it shows that an interpretation of our results in terms of only moderately sub-solar metallicities, coupled with modest dust reddening, is at least physically plausible within the magnitude range probed to date, and that the long-anticipated population of really metal-poor dust-free objects possibly lies at much fainter magnitudes than originally suggested by the early results of Bouwens et al. (2010b). In addition, it serves to remind us that the theoretically-predicted scatter in β at these epochs is on a completely different scale to that seen in our raw individual galaxy β distributions, the latter being still utterly dominated by the impact of photometric errors (compare, for example, Fig. 7 and Fig. 1). Nevertheless, Fig. 7 also provides strong continued motivation for pushing the robust measurement of $\langle \beta \rangle$ to ever fainter galaxy luminosities in the young Universe.

5.4 Implications for reionization

A full analysis of the implications of the combined results of the UDF12 programme for our understanding of cosmic reionization is presented by Robertson et al. (2013). This analysis will necessarily draw on the new luminosity-function measurements presented by McLure et al. (2013) and Schenker et al. (2013), and on the new measurements of $\langle \beta \rangle$ presented here, because determining the ability of the emerging galaxy population at $z = 6 - 9$ to reionize the Universe requires knowledge not only of the number density of the galaxies, but also information on their ability to supply the required ionizing photons. As discussed in Section 1, the ability of a given galaxy to contribute to the ionization of the surrounding intergalactic medium depends on its luminosity, the age and metallicity of its stellar population, and the escape fraction of ionizing photons

Unfortunately, the relatively modest values of $\langle \beta \rangle$ found in the present study do not easily lend themselves to straightforward interpretation. In particular, Fig. 6 suggests that there is little prospect of using our new measurements of $\langle \beta \rangle$ to set new constraints on the ionizing-photon escape fraction, f_{esc} , without significant additional information (e.g. a meaningful estimate of the contribution of nebular emission lines to the rest-frame optical colours, as measured by *Spitzer* IRAC; e.g., Stark et al. 2013; Labbé et al. 2013).

On the other hand, the degeneracy between metallicity and dust obscuration is somewhat less of an issue for reionization calculations than for calculations of cosmic star-formation rate density, as the former concerned only with the UV photons which survive to exit a galaxy and potentially contribute to cosmic reionization. Moreover, our finding that $\langle \beta \rangle$ remains close to $\beta = -2$ at $z \simeq 7, 8$ and even $z \simeq 9$ suggests that the galaxies detected to date already contain relatively mature, metal-enriched stellar populations, lending support to a picture in which star-formation (and hence cosmic reionization) commenced at significantly higher redshifts.

6 CONCLUSIONS

We have used the new ultra-deep, near-infrared imaging of the HUDF provided by our UDF12 HST WFC3/IR imaging campaign to explore the rest-frame UV properties of galaxies at redshifts $z > 6.5$. In this study we have exploited the final multi-band WFC3/IR imaging (UDF12+UDF09) to select deeper and more reliable galaxy samples at $z \simeq 7$, $z \simeq 8$, and $z \simeq 9$, and to provide improved photometric redshifts. Most importantly, we have used the enhanced dataset to provide more accurate photometry, and to base galaxy selection primarily on the new J_{140} imaging, which exerts minimal influence on the derivation of the UV spectral index β ($f_\lambda \propto \lambda^\beta$) from either $J_{125} - H_{160}$ colour (e.g. Bouwens et al. 2010b; Dunlop et al. 2012), or $J_{125} + J_{140} + H_{160}$ power-law fitting (as advocated by Rogers et al. 2013). Our main results are as follows.

i) We have produced the first robust and unbiased measurement of the average UV power-law index, $\langle\beta\rangle$, ($f_\lambda \propto \lambda^\beta$) for faint galaxies at $z \simeq 7$, finding $\langle\beta\rangle = -2.1 \pm 0.2$ at $z \simeq 7$ for galaxies with $M_{UV} \simeq -18$. This result means that the faintest galaxies uncovered to date at this epoch have, *on average*, UV colours no more extreme than those displayed by the bluest star-forming galaxies found in the low-redshift Universe.

ii) We have made the first meaningful measurements of $\langle\beta\rangle$ at $z \simeq 8$, finding a similar value, $\langle\beta\rangle = -1.9 \pm 0.3$.

iii) We have offered a tentative first estimate of $\langle\beta\rangle$ at $z \simeq 9$ (based on the $J_{140} - H_{160}$ colours of the six galaxies in the redshift range $8.5 < z < 10$ reported in Ellis et al. 2013), and find $\langle\beta\rangle = -1.8 \pm 0.6$, essentially unchanged from $z \simeq 6-7$ (albeit highly uncertain).

iv) Finally, we have used careful end-to-end source injection+retrieval+analysis simulations to quantify any small residual biases in our measurements, and to test for any evidence for significant intrinsic scatter in the β values displayed by the galaxies in the faintest luminosity bin which we can study at $z \simeq 7$. While models including a range of β values provide a modestly-improved description of the data, we find that there is, as yet, no evidence for a significant *intrinsic* scatter in β within our new $z \simeq 7$ galaxy sample.

Our results exclude the possibility that even our faintest galaxy samples contain a substantial population of very low-metallicity, dust-free objects with $\beta \simeq -3$. Rather, our findings are most easily explained by a population of steadily star-forming galaxies with either \simeq solar metallicity and zero dust, or moderately sub-solar ($\simeq 10 - 20\%$) metallicity with modest dust obscuration ($A_V \simeq 0.1 - 0.2$). This latter interpretation is consistent with the predictions of a state-of-the-art galaxy-formation simulation, which also suggests that a significant population of very-low metallicity, dust-free galaxies with $\beta \simeq -2.5$ may not emerge until $M_{UV} > -16$, a regime likely to remain inaccessible until the JWST.

ACKNOWLEDGEMENTS

JSD and PD thank their collaborators U. Maio and B. Ciardi for making available the SPH simulations utilised in Section 5.3. JSD, PD, VW, RAAB, and TAT acknowledge the support of the European Research Council via the award of an Advanced Grant. JSD and RJM acknowledge the support of the Royal Society via a Wolf-

son Research Merit Award, and a University Research Fellowship respectively. ABR and EFCL acknowledge the support of the UK Science & Technology Facilities Council. US authors acknowledge financial support from the Space Telescope Science Institute under award HST-GO-12498.01-A. SRF is partially supported by the David and Lucile Packard Foundation. SC acknowledges the support of the European Commission through the Marie Curie Initial Training Network ELIXIR. This work is based in part on observations made with the NASA/ESA *Hubble Space Telescope*, which is operated by the Association of Universities for Research in Astronomy, Inc, under NASA contract NAS5-26555. This work is also based in part on observations made with the *Spitzer Space Telescope*, which is operated by the Jet Propulsion Laboratory, California Institute of Technology under NASA contract 1407.

REFERENCES

- Arnouts S., Cristiani S., Moscardini L., Matarrese S., Lucchin F., Fontana A., Giallongo E., 1999 MNRAS, 310, 540
 Beckwith S.V.W., et al., 2006, AJ, 132, 1729
 Bertin E., Arnouts S., 1996, A&AS, 117, 393
 Bianchi S., Schneider R., 2007, MNRAS, 378, 973
 Bouwens R.J., et al., 2009, ApJ, 705, 936
 Bouwens R.J., et al., 2010a, ApJ, 709, L113
 Bouwens R.J., et al., 2010b, ApJ, 708, L69
 Bouwens R.J., et al., 2011, ApJ, 737, 90
 Bouwens R.J., et al., 2012, ApJ, 754, 83
 Bradley L.D., et al., 2012, ApJ, 760, 108
 Bromm V., Loeb A., 2003, Nature, 425, 812
 Bromm V., Yoshida N., Hernquist L., McKee C.F., 2009, Nature, 459, 49
 Bruzual G., Charlot S., 2003, MNRAS, 344, 1000
 Bunker A.J., et al., 2010, MNRAS, 409, 955
 Calzetti D., Kinney A.L., Storchi-Bergmann T., 1994, ApJ, 429, 582
 Calzetti D., Armus L., Bohlin R.C., Kinney A.L., Koornneef J., Storchi-Bergmann T., 2000, ApJ, 533, 682
 Castellano M., et al., 2012, A&A, 540, 39
 Campisi M.A., Maio U., Salvaterra R., Ciardi B., 2011, MNRAS, 416, 2760
 Coe D., et al., 2013, ApJ, 762, 32
 Dayal P., Ferrera A., 2012, MNRAS, 421, 2568
 Dayal P., Ferrara A., Saro A., 2010, MNRAS, 402, 1449
 Dayal P., Dunlop J.S., Maio U., Ciardi B., 2013, MNRAS, in press (arXiv:1211.1034)
 Dolag K., Borgani S., Murante G., Springel V., 2009, MNRAS, 399, 497
 Dunlop J.S., 2012, arXiv:1205.1543
 Dunlop J.S., McLure R.J., Robertson B.E., Ellis R.S., Stark D.P., Cirasuolo M., de Ravel L., 2012, MNRAS, 420, 901
 Ellis R.S., et al., 2013, ApJL, 763, L7
 Erb D.K., Pettini M., Shapley A., Steidel C.C., Law D.R., Reddy N.A., 2010, ApJ, 719, 1168
 Finkelstein S.L., Papovich C., Giallisco M., Reddy N.A., Ferguson H.C., Koekemoer A.M., Dickinson M., 2010, ApJ, 719, 1250
 Finkelstein S.L., et al., 2012, ApJ, 756, 164
 Gonzalez-Perez V., Lacey C.G., Baugh C.M., Frenk C.S., Wilkins S.M., 2013, MNRAS, 429, 1609
 Grazian A., et al., 547, 51
 Grogin N.A., et al., 2011, ApJS, 197, 35
 Hathi N.P., Malhotra S., Rhoads J.E., 2008, ApJ, 673, 686
 Heger A., Woosley S.E., 2002, ApJ, 567, 532
 Heinis S., et al., 2013, MNRAS, 429, 1113
 Ilbert O., et al., 2006 A&A, 457, 841
 Koekemoer A.M., et al., 2011, ApJS, 197, 36
 Koekemoer A.M., et al., 2013, ApJS, in press (arXiv:1212.1448)
 Labbé I., et al., 2013, ApJL, submitted (arXiv:1209.3037)
 Leitherer C., Heckman T.M., 1995, ApJS, 96, 9
 Leitherer C. et al., 1999, ApJS, 123, 3

- Maio U., Dolag K., Ciardi B., Tornatore L., 2007, MNRAS, 379, 963
- Maio U., Ciardi B., Yoshida N., Dolag K., Tornatore L., 2009, A&A, 503, 25
- Maio U., Ciardi B., Dolag K., Tornatore L., Khochfar S., 2010, MNRAS, 407, 1003
- Maio U., Khochfar S., Johnson J.L., Ciardi B., 2011, MNRAS, 414, 1145
- Maiolino R., et al., 2006, MmSAI, 77, 643
- McLure R.J., Dunlop J.S., Cirasuolo M., Koekemoer A.M., Sabbi E., Stark D., Targett T.A., Ellis R.S., 2010, MNRAS, 403, 960
- McLure R.J., et al., 2011, MNRAS, 418, 2074
- McLure R.J., et al., 2013, MNRAS, in press (arXiv:1212.5222)
- Meurer G.R., Heckman T.M., Calzetti D., 1999, ApJ, 521, 64
- Mitra S., Ferrara A., Choudhury, T. Roy, 2013, MNRAS, 428, L1
- Nagao T., et al., 2008, ApJ, 680, 100
- Oesch P.A., et al., 2010, ApJ, 709, L16
- Oesch P.A., et al., 2012, ApJ, 759, 135
- Oke J.B., 1974, ApJS, 27, 21
- Paardekooper J.-P., Khochfar S., Dalla Vecchia C., 2013, MNRAS, 429, L94
- Padovani P., Matteucci F., 1993, ApJ, 416, 26
- Pawlik A.H., Milosavljevic M., Bromm V., 2011, ApJ, 731, 54
- Reddy N., et al., 2012, ApJ, 744, 154
- Robertson B.E., Ellis R.S., Dunlop J.S., McLure R.J., Stark D., 2010, Nat, 468, 49
- Robertson B.E., et al., 2013, ApJ, in press (arXiv:1301.1228)
- Rogers A.B., McLure R.J., Dunlop J.S., 2013, MNRAS, 429, 2456
- Salvaterra R., Ferrara A., Dayal P., 2011, MNRAS, 414, 847
- Schaerer D., 2002, A&A, 382, 28
- Schenker M.A., et al., 2012, ApJ, 744, 179
- Springel V., Yoshida N., White S.D.M., 2001, New A, 6, 79
- Springel V., 2005, MNRAS, 364, 1105
- Springel V., Hernquist L., 2003, MNRAS, 339, 289
- Stark D.P., Schenker M.A., Ellis R.S., Robertson B., McLure R.J., Dunlop J.S., 2013, ApJ, 764, 195
- Stratta G., Maiolino R., Fiore F., D'Elia V., 2007, ApJ, 661, 9
- Thielemann F.-K. et al., 2003, Nuclear Physics A, 718, 139
- Tokunaga A.T., Vacca W.D., 2005, PASP, 117, 1459
- Tornatore L., Ferrara A., Schneider R., 2007, MNRAS, 382, 945
- van den Hoek L.B., Groenewegen M.A.T., 1997, A&AS, 123, 305
- Wilkins S.M., Bunker A.J., Stanway E., Lorenzoni S., Caruana J., 2011, MNRAS, 417, 717
- Wilkins S., Gonzalez-Perez V., Lacey C.G., Baugh C.M., 2012, MNRAS, 424, 1284
- Woosley S.E., Weaver T.A., 1995, ApJS, 101, 181
- Yoshida N., Abel T., Hernquist L., Sugiyama N., 2003, ApJ, 592, 645
- Zheng W., et al., 2012, Nature, 489, 406

APPENDIX A: UV SLOPE (β) MEASUREMENTS FOR INDIVIDUAL OBJECTS

In this appendix we provide a table of the key measured/derived properties (positions, photometric redshifts, absolute magnitudes, and UV slopes β) of the objects analysed to produce the plots and statistical averages in this paper. The sample summarised in Table A1 comprises the subset of the HUDF12 $z_{phot} = 6.4 - 8.4$ sample which survived the J_{140} selection threshold described in Section 2.2, supplemented by a small number of brighter objects from the two UDF Parallel fields.

Table A1. Positions, photometric redshifts, absolute UV magnitudes, and β values for the objects analysed in this paper. We give both the simple $J - H$ colour determinations of β , and our preferred optimal power-law determinations, the latter with errors. We caution that, given the typical sizes of these errors, individual measurements of β must be regarded as highly uncertain. Sources are ordered by photometric redshift (see McLure et al. 2013), with the source name in column 1 indicating whether the source lies within the UDF itself, or the parallel fields UDFPar1 and UDFPar2.

Name	RA(J2000)	Dec(J2000)	z_{phot}	M_{1500}	β_{J-H}	$\beta_{PL} \pm 1\sigma$
UDF12-3732-6420	03:32:37.32	-27:46:42.0	6.4	-17.4	-4.0	-3.6 \pm 1.5
UDF12-3983-6189	03:32:39.83	-27:46:18.9	6.4	-17.7	-1.8	-1.8 \pm 1.1
UDF12-3677-7536	03:32:36.77	-27:47:53.6	6.4	-18.8	-2.2	-2.1 \pm 0.7
UDF12-3696-5536	03:32:36.96	-27:45:53.6	6.5	-17.3	-2.3	-2.3 \pm 1.2
UDF12-4058-5570	03:32:40.58	-27:45:57.0	6.5	-17.8	-1.3	-1.3 \pm 1.1
UDF12-3900-6482	03:32:39.00	-27:46:48.2	6.5	-17.9	-0.2	-0.3 \pm 0.7
UDF12-3638-7163	03:32:36.38	-27:47:16.3	6.5	-18.5	-2.3	-2.3 \pm 0.6
UDF12-4056-6436	03:32:40.56	-27:46:43.6	6.5	-18.5	-1.5	-1.9 \pm 0.6
UDFPar2-0194-2033	03:33:01.94	-27:52:03.3	6.5	-19.3	-1.6	-1.7 \pm 0.3
UDF12-3865-6041	03:32:38.65	-27:46:04.1	6.5	-17.6	-3.8	-3.6 \pm 1.2
UDF12-4472-6362	03:32:44.72	-27:46:36.2	6.5	-17.9	0.8	0.4 \pm 1.1
UDF12-4268-7073	03:32:42.68	-27:47:07.3	6.5	-18.1	-2.0	-2.0 \pm 0.6
UDF12-3736-6245	03:32:37.36	-27:46:24.5	6.6	-17.6	-2.5	-2.5 \pm 1.1
UDF12-4182-6112	03:32:41.82	-27:46:11.2	6.6	-17.8	-3.6	-3.5 \pm 0.7
UDF12-4219-6278	03:32:42.19	-27:46:27.8	6.6	-18.9	-2.1	-2.1 \pm 0.6
UDF12-4256-7314	03:32:42.56	-27:47:31.4	6.6	-19.3	-2.1	-2.2 \pm 0.6
UDFPar2-0977-0485	03:33:09.77	-27:50:48.5	6.6	-19.1	-0.5	-0.8 \pm 0.3
UDF12-3734-7192	03:32:37.34	-27:47:19.2	6.7	-17.8	-3.0	-3.0 \pm 1.1
UDF12-3675-6447	03:32:36.75	-27:46:44.7	6.7	-17.9	-2.4	-2.4 \pm 0.7
UDF12-4160-7045	03:32:41.60	-27:47:04.5	6.7	-18.3	-2.3	-2.3 \pm 0.6
UDF12-3836-6119	03:32:38.36	-27:46:11.9	6.7	-18.5	-2.1	-1.6 \pm 0.7
UDFPar2-1044-1081	03:33:10.44	-27:51:08.1	6.7	-18.5	-2.4	-2.1 \pm 0.6
UDF12-3471-7236	03:32:34.71	-27:47:23.6	6.7	-17.4	-0.1	-0.2 \pm 0.9
UDF12-4068-6498	03:32:40.68	-27:46:49.8	6.7	-17.5	-3.0	-2.9 \pm 1.1
UDF12-3975-7451	03:32:39.75	-27:47:45.1	6.7	-17.7	-1.1	-1.3 \pm 1.1
UDF12-3744-6513	03:32:37.44	-27:46:51.3	6.7	-18.8	-2.7	-2.7 \pm 0.7
UDFPar1-5693-0509	03:32:56.93	-27:40:50.9	6.7	-18.7	-3.5	-2.6 \pm 0.5
UDF12-3729-6175	03:32:37.29	-27:46:17.5	6.8	-17.9	-0.8	-0.7 \pm 0.8
UDF12-3958-6565	03:32:39.58	-27:46:56.5	6.8	-18.7	-1.8	-1.8 \pm 0.6
UDFPar2-0419-0314	03:33:04.19	-27:50:31.4	6.8	-20.1	-1.5	-1.5 \pm 0.3
UDF12-3989-6189	03:32:39.89	-27:46:18.9	6.8	-17.8	-3.1	-3.0 \pm 1.0
UDF12-4431-6452	03:32:44.31	-27:46:45.2	6.8	-18.5	-3.3	-3.3 \pm 0.6
UDFPar2-0914-1531	03:33:09.14	-27:51:53.1	6.8	-18.5	-2.4	-2.4 \pm 0.4
UDF12-3456-6494	03:32:34.56	-27:46:49.4	6.8	-17.6	-0.5	-0.5 \pm 1.0
UDF12-4105-7156	03:32:41.05	-27:47:15.6	6.8	-18.7	-1.4	-0.9 \pm 0.6
UDFPar1-0210-1463	03:33:02.10	-27:41:46.3	6.8	-19.3	-1.8	-1.9 \pm 0.3
UDFPar2-0119-1134	03:33:01.19	-27:51:13.4	6.8	-19.1	-1.5	-1.5 \pm 0.3
UDFPar1-5881-0386	03:32:58.81	-27:40:38.6	6.9	-18.5	-2.7	-2.7 \pm 0.5
UDFPar1-0243-1313	03:33:02.43	-27:41:31.3	6.9	-19.3	-1.7	-2.0 \pm 0.3
UDFPar2-0631-1217	03:33:06.31	-27:51:21.7	6.9	-18.7	-2.1	-2.1 \pm 0.5
UDF12-4256-6566	03:32:42.56	-27:46:56.6	7.0	-20.0	-1.4	-1.4 \pm 0.6
UDFPar2-0964-0508	03:33:09.64	-27:50:50.8	7.0	-20.3	-1.8	-2.3 \pm 0.3
UDFPar2-0914-1555	03:33:09.14	-27:51:55.5	7.0	-19.5	-1.6	-2.6 \pm 0.3
UDFPar2-0704-0555	03:33:07.04	-27:50:55.5	7.0	-19.3	-1.7	-1.7 \pm 0.3
UDF12-4245-6534	03:32:42.45	-27:46:53.4	7.0	-17.1	0.4	-0.2 \pm 1.6
UDF12-4071-7347	03:32:40.71	-27:47:34.7	7.0	-17.5	-2.4	-2.3 \pm 1.5
UDF12-3431-7115	03:32:34.31	-27:47:11.5	7.0	-18.2	-0.6	-0.6 \pm 0.7
UDF12-3825-6566	03:32:38.25	-27:46:56.6	7.0	-17.2	-0.3	-0.8 \pm 1.6
UDF12-3853-7519	03:32:38.53	-27:47:51.9	7.0	-17.8	-3.4	-3.3 \pm 1.2
UDFPar1-5897-0504	03:32:58.97	-27:40:50.4	7.0	-19.3	-1.7	-1.7 \pm 0.3
UDFPar1-5959-1209	03:32:59.59	-27:41:20.9	7.0	-19.4	-2.0	-2.1 \pm 0.3
UDFPar1-5670-1082	03:32:56.70	-27:41:08.2	7.0	-19.6	-1.9	-1.6 \pm 0.2
UDFPar2-0540-1189	03:33:05.40	-27:51:18.9	7.0	-19.1	-2.3	-2.5 \pm 0.4
UDFPar1-5969-0353	03:32:59.69	-27:40:35.3	7.1	-19.7	-2.3	-2.3 \pm 0.3
UDFPar1-5850-0239	03:32:58.50	-27:40:23.9	7.1	-19.2	-2.4	-2.5 \pm 0.4
UDF12-4242-6243	03:32:42.42	-27:46:24.3	7.2	-18.1	-1.5	-1.6 \pm 0.6
UDF12-3402-6504	03:32:34.02	-27:46:50.4	7.2	-18.2	-3.3	-3.1 \pm 0.7
UDF12-4242-6137	03:32:42.42	-27:46:13.7	7.2	-17.8	-0.6	-0.8 \pm 1.2
UDF12-4384-6311	03:32:43.84	-27:46:31.1	7.3	-17.7	-3.5	-3.3 \pm 1.3
UDF12-3668-8067	03:32:36.68	-27:48:06.7	7.3	-17.9	-4.0	-3.6 \pm 1.2
UDF12-3973-6214	03:32:39.73	-27:46:21.4	7.3	-18.2	-3.6	-3.6 \pm 0.8

Table A1. cont.

Name	RA(J2000)	Dec(J2000)	z_{phot}	M_{1500}	β_{J-H}	$\beta_{PL} \pm 1\sigma$
UDFPar1-5575-1070	03:32:55.75	-27:41:07.0	7.3	-19.1	-0.9	-0.9±0.5
UDF12-3313-6545	03:32:33.13	-27:46:54.5	7.3	-18.4	-2.2	-2.2±0.6
UDFPar1-5973-1193	03:32:59.73	-27:41:19.3	7.4	-19.3	-1.7	-2.0±0.4
UDF12-3885-7540	03:32:38.85	-27:47:54.0	7.5	-17.9	-2.2	-2.2±1.0
UDF12-3931-6181	03:32:39.31	-27:46:18.1	7.5	-18.0	-4.0	-3.9±1.0
UDF12-3880-7072	03:32:38.80	-27:47:07.2	7.5	-19.9	-1.4	-1.4±0.6
UDFPar1-5939-2017	03:32:59.39	-27:42:01.7	7.5	-18.9	-1.0	-1.3±0.7
UDFPar2-0376-1197	03:33:03.76	-27:51:19.7	7.5	-20.0	-1.5	-1.6±0.4
UDFPar2-0378-1204	03:33:03.78	-27:51:20.4	7.5	-20.4	-1.1	-1.4±0.3
UDF12-4470-6443	03:32:44.70	-27:46:44.3	7.7	-19.4	-1.8	-1.9±0.7
UDF12-4288-6345	03:32:42.88	-27:46:34.5	7.7	-18.7	-1.4	-1.4±0.8
UDF12-3722-8061	03:32:37.22	-27:48:06.1	7.7	-18.9	-1.9	-1.9±0.7
UDF12-3952-7174	03:32:39.52	-27:47:17.4	7.7	-19.0	-0.7	-0.7±0.7
UDFPar2-0464-0530	03:33:04.64	-27:50:53.0	7.7	-19.6	-2.1	-2.0±0.4
UDF12-4309-6260	03:32:43.09	-27:46:26.0	7.7	-18.1	-2.2	-2.2±0.8
UDF12-3939-7040	03:32:39.39	-27:47:04.0	7.7	-18.2	-1.2	-1.3±0.8
UDF12-4474-6449	03:32:44.74	-27:46:44.9	7.8	-18.3	-2.9	-2.8±0.7
UDF12-3911-6493	03:32:39.11	-27:46:49.3	7.8	-17.8	-2.8	-2.8±1.2
UDF12-3344-6598	03:32:33.44	-27:46:59.8	7.8	-17.9	-2.7	-2.7±1.0
UDFPar1-5644-1009	03:32:56.44	-27:41:00.9	7.8	-19.2	-2.5	-2.5±0.7
UDF12-4308-6277	03:32:43.08	-27:46:27.7	8.0	-18.2	-3.6	-3.7±0.9
UDF12-3780-6001	03:32:37.80	-27:46:00.1	8.0	-18.7	-2.4	-2.4±0.7
UDF12-3813-5540	03:32:38.13	-27:45:54.0	8.1	-18.9	-1.4	-1.6±0.6
UDF12-3763-6015	03:32:37.63	-27:46:01.5	8.3	-18.5	-1.9	-2.3±0.7